Version of Record: https://www.sciencedirect.com/science/article/pii/S0168583X19300916
Manuscript_c2d6a85cff7c10919304cefaa7148e6e

Raman investigation of ion irradiated TiC and ZrC ~~upon MeV ion irradiation~~

S. Pellegrino[1], P. Trocellier[2], L. Thomé[3], S. Miro[2], J-M. Costantini[4], E. Jouanny[4]

1 CEA, INSTN, UEPTN, Laboratoire JANNUS, F-91191 Gif-sur-Yvette, France

2 CEA, DEN, Service de Recherches de Métallurgie Physique, Laboratoire JANNUS, F-91191 Gif-sur-Yvette, France

3 CNRS, CSNSM, IN2P3, F-91400 Orsay, France

4 CEA, DEN, Service de Recherches de Métallurgie Appliquée, F-91191 Gif-sur-Yvette, France

Abstract

Single crystals of transition metal carbides from group IV, TiC_{1-x} and ZrC_{1-x}, have been irradiated at room temperature (RT) with 1.2 MeV gold ions for various fluences in the range 2×10^{14} - 3×10^{16} ions/cm^2 and polycrystals for fluences between 2×10^{13} and 4×10^{15} ions/cm² ~~also at RT~~. The irradiated samples were ~~then~~ characterized by micro Raman spectroscopy. For this purpose, the evolution of main parameters of Raman spectra for both types of samples (~~peak~~ band positions, shifts, and intensities, and optical over acoustical band area ratios) versus ~~gold~~ ion fluence are reported, ~~compared~~ and discussed. All acoustic~~al~~ and optical bands increase and broaden with fluence. Yet no amorphization is achieved under the highest fluence for both carbides. From the lowest fluence up to 10^{15} ions/cm², point defects like interstitials and vacancies are created. The increasing number of carbon vacancies involves a local variation in stoichiometry accompanied by carbon release. For fluence above 10^{15} ions/cm², ~~other type of~~ extended defects ~~(and bigger)~~ like dislocation loops ~~and dislocation network~~ appear, as ~~confirmed~~ seen by TEM observations.

1. Introduction

In nuclear reactors of the next generation, materials will be submitted to severe conditions such as elevated temperature and high level of radiation damage. Transition metal ceramics such as TiC and ZrC have been selected as candidates for fuel matrices (ZrC especially for use as tri-structural-isotropic fuel particles: TRISO) in future high temperature gas cooled reactors (HTGR) [1]. These ceramics are also considered as potential first wall materials for fusion technology [2-3], thanks to their outstanding characteristics, such as refractory behavior, high temperature stability (melting temperature higher than 3000°C), high mechanical resistance, small neutron capture cross sections, and good fission product confinement capability.

In group IV transition metal carbides, the overlap of 3- (or 4) d_{z^2} and $d_{x^2} - d_{y^2}$ orbitals of the metal atoms with 2p orbitals of the non-metal atoms is known to induce a σ hybridization. The diagrams describing the ~~phonon~~vibrational density of state (VDOS) of TiC and ZrC have been calculated by authors [4] [~~4-9~~]. ~~All these DOS diagrams are characterized by the presence of four well separated peak blocks located from both sides of the Fermi level and combining partial DOS from Ti 3d (Zr 4d) and C 2p orbitals [4].~~ Group IV transition metal carbides crystallize in the rock-salt structure. For stoichiometric compounds, each atom occupies a symmetry inversion site leading to an O_h symmetry. Due to this fact, the first order Raman scattering is strictly forbidden. However, the presence of C vacancies in sub-stoichiometric cubic phase (M(IV) $X_{(1-x)}$ with M = Ti, Zr, and X = C) modifies the O_h symmetry. As a result, these structural defects render first order Raman active by breaking the usual q = 0 phonon wave vector selection rule [5]. A careful literature survey allows us identifying a small number of Raman studies devoted to TiC and ZrC compounds [6-13]. They are essentially related to stoichiometry variations, but not to the consequences of

radiation damage. The most relevant result derived from these papers is that the stoichiometry deviation plays a major role on the shape of the Raman spectrum. Therefore, we have undertaken micro-Raman characterization of transition metal carbides in order to describe the chemical environments existing in sub-stoichiometric TiC and ZrC compounds, and evaluate their possible evolution under ion irradiation [14, 15].

2. State of knowledge

~~2.1 TiC and ZrC behavior under irradiation~~

2.1.1 TiC

A 100 keV electron irradiation of a <100> $TiC_{0.93}$ thin foil at room temperature with a dose rate of $10^{19}/cm^2/s$ (0.002 dpa/s) for 215 minutes induces the apparition of both an ordered cubic superstructure $TiC_{0.5}$ and graphite [16].

The first ion irradiation experiments of TiC are due to Hojou [22-24]. Low-energy (20 – 25 keV) molecular ion beams of hydrogen and deuterium were used at 18 K and the evolution of the microstructure was followed by *in situ* TEM investigations. Amorphization was observed for H_2^+ irradiation at ~10^{17} cm^{-2}, while no amorphization has been detected for D_2^+ irradiation at 4.5×10^{17} cm^{-2}, probably due to the difficulty to create Ti–D and/or C–D bonds. Ti-H and C-H chemical bonds prevent the recovery of irradiation defects, leading to amorphization [17-18]. Helium ion irradiation was carried out from RT to 1423 °K at 20 keV, after 25 keV H_2^+ pre-injection or simultaneous dual beam implantation [19]. The He ion fluence was varied from 1.5 to 9×10^{17} cm^{-2} for a flux of 2.5×10^{14} $cm^{-2}s^{-1}$. No amorphization is detected. Helium bubble formation occurred but the bubble growth was limited to 1–2 nm at RT and 7–8 nm at 1423 °K.

Proton irradiations were conducted using three doses (0.17, 0.34, and 0.80 dpa) for three temperatures (600°C, 800°C, and 900°C), and the samples were examined by TEM to evaluate the irradiation-induced microstructures [20]. The main feature observed was the formation of mainly unfaulted aggregate defects and Frank-type dislocation loops. Moreover, the evolution of the loop sizes and densities versus temperature suggested an increase of the vacancy mobility above 800°C due to carbon vacancy reordering in the Ti lattice.

2.1.2 ZrC

Taubin et al. performed neutron irradiation of $ZrC_{0.96}$ up to 4×10^{16} cm^{-2} with a fast neutron component (E > 1 MeV). Two neutron fluxes were chosen: 4.8×10^{14} and 3.3×10^{15} $cm^{-2}s^{-1}$. The maximum temperature of the sample did not exceed 700 °K. The thermal conductivity, the thermal expansion, the heat capacity and the specific electric resistivity were simultaneously measured during irradiation [21, 22]. It was shown that the thermal conductivity increases while the thermal expansion, the heat capacity and the electrical resistivity decrease with increasing neutron fluence for both flux values. Moreover, a strong recovery is reached after irradiation in a very short time (less than 5 minutes) essentially due to the mobility of defects.

Gosset et al. carried out 4 MeV Au ion irradiation of ZrC polycrystals for fluences from 10^{11} to 5×10^{15} cm^{-2} at RT [23, 24]. Three damage stages were determined using TEM investigations: (i) at low fluence (<10^{12} cm^{-2}), only very small modifications are observed; (ii) at intermediate fluence, micro-strains appear together with small faulted dislocation loops; (iii) at the highest fluence used (>10^{14} cm^{-2}), the micro-strains reach a maximum and the loops coalesced to form a dense dislocation network. A moderate cell parameter increase, corresponding to 0.6 % volume swelling is found. These results show that the irradiation behavior of ZrC is similar to cubic metals.

Jian Gan et al. irradiated ZrC with two types of particles: 1 MeV Kr ions to doses of 10 and 30 dpa at 27°C or 10 to 70 dpa at 800°C with a damage rate approximately 3.0×10^{-3} dpa/s [25]; 2.6 MeV protons at 800°C to a fluence of 2.75×10^{19} cm^{-2}, corresponding to 1.8 dpa [26]. In the case of Kr ion irradiation, no radiation-induced amorphization was found and a lattice expansion of approximately 7 % was observed at 800°C for a dose of 70 dpa. In the case of proton irradiation, no change of lattice constant can be detected. Proton irradiation for 1.8 dpa exhibits less radiation damage than Kr ion irradiation. Moreover, faulted loops were observed in the proton-irradiated sample and not in the Kr-ion irradiated one.

Fast neutron irradiation (E>0.1 MeV) was carried for high purity $ZrC_{0.93}$ in dose and temperature ranges of $1–10\times10^{21}$ cm^{-2} and 635–1480°C, respectively [27]. It was shown that this ceramic is quite stable in these conditions; small dislocation loops were observed at 670°C evolving to Frank loops at 1280°C and transforming in prismatic loops around 1480°C. Reynolds et al. [28] irradiated four experimental fuel particle types based on zirconium carbide (with porous and dense pyrocarbon coatings) with fast neutrons (E > 0.18 MeV) at 1200°C up to 5×10^{21} cm^{-2}. Stereoscopic, metallographic and electron-beam microprobe examination of the irradiated particles showed that ZrC possesses exceptional resistance to chemical attack by fission products and good mechanical stability under irradiation.

An *ab initio* study of point defects in ZrC showed that: (i) C vacancies can easily be formed; (ii) C interstitials are the most stable interstitial defects since they form trimers along the <101> direction. By contrast, antisite defects or Zr vacancies or interstitials were shown to be dramatically less stable [29].

Recent reviews were published concerning the irradiation behavior of ZrC in the aim of nuclear fuel applications [30-32]. Ion irradiations conducted even at low temperature (~20°K) clearly demonstrate that ZrC is very resistant to amorphization, likely because chemical disordering is very difficult to introduce in the lattice. It also appears that strength and creep

(thermal and under irradiation) at elevated temperatures are among the critical properties which are largely missing at present from the literature survey.

The ~~in-depth~~ thermal conductivity depth profile of 2.6 MeV proton-irradiated $ZrC_{1.01}$ polycrystals has been directly measured using scanning thermal microscopy (SThM) by Jensen et al. [33]. This method has been used for the first time to map the thermal conductivity (k) profile of cross section of proton-irradiated ZrC sample. The measured profile is independent of topography. They found a value greater than 66% reduction of k between the damaged and undamaged material, most likely due to heat carrier scattering from the large dislocation loops.

The effect of the stoichiometry on the damage evolution in proton-irradiated ZrC_x at 800°C up to a dose of 3 dpa (dose rate: 4.7×10^{-5} dpa/s and flux: 1×10^{18} ions/cm^2 /s) was studied with x varying in the 0.9-1.2 range [34]. A high density of dislocation loops was observed by TEM. The loop size and density are both dependent on the dose and on the stoichiometry. $ZrC_{1.2}$ shows a quite different behavior as compared to the lower C-ratio stoichiometries. However, no irradiation-induced voids were observed in any sample.

Recently, Pellegrino et al. have studied the radiation response of TiC and ZrC single crystals irradiated in the nuclear energy loss regime (1.2 MeV Au ions), and have compared the results to those obtained on SiC [35, 36]. The evolution of the microstructure of carbides versus ion fluence was followed by combining RBS/C, XRD and TEM. At the lowest Au fluence used (2.8×10^{14} cm^{-2}, corresponding to 1.3 dpa), the accumulation of defects created by nuclear collisions leads to the amorphization of SiC. In contrast, TiC and ZrC do not amorphize up to Au ion fluence of 3.3×10^{15} cm^{-2} (corresponding to 13.6 dpa for TiC and 20 dpa for ZrC). The authors assumed that the pronounced metallic character of the Ti–C/Zr–C bonds may play a major role to explain this difference in the radiation tolerance of ZrC and TiC as compared to SiC. Hobbs and coworkers [37] highlighted some criteria, such as the type of structure, the

ionicity, the melting point and the homologous crystallization temperature, for the occurrence of the crystalline-amorphous phase transformation.

~~2.2 Raman characterization of group IV carbides~~

~~A Raman spectrum can be described as the response in terms of atomic vibrations of a crystal lattice excited by a photon probe. The phonons have two main origins [11, 13]:~~

- ~~Acoustic phonons correspond to coherent movements of metallic atoms (Ti or Zr) of the lattice out of their equilibrium positions. These displacements may occur in the same direction as the phonon propagation (longitudinal phonons: LA) or perpendicularly to the propagation (transverse phonons: TA);~~
- ~~Optical phonons are out-of-phase movements of the non-metal atoms (C) in the lattice occurring when the lattice is made of non-equivalent atoms in the unit cell. As in the case of acoustic phonons, the displacements may occur in the same direction as the phonon propagation (longitudinal phonons: LO) or perpendicularly to the propagation (transverse phonons: TO).~~

~~It is worth mentioning that~~

3. Experimental

TiC and ZrC single crystals (from MaTecK-Germany) and polycrystals (from CEA) were implanted with 1.2 MeV Au^{2+} ions at room temperature using the JAPET™ 2 MV Pelletron™ TANDEM at the JANNuS Laboratory CEA Saclay [42]. Ion fluences ranged from 2×10^{14} to 3×10^{16} cm^{-2} for single crystals and from 2×10^{13} to 4×10^{15} cm^{-2} for polycrystals. The

respective values of the projected ion ranges were ~150 nm for TiC and ~140 nm for ZrC (see table 1 calculated by SRIM [43]).

Raman characterizations were carried out with a Renishaw Invia Reflex device equipped with a Leica DM2500 microscope (×100 objective) at the JANNuS laboratory in Saclay. Raman scattering measurements were performed using the 532 nm line of a frequency-doubled Nd-YAG laser with an output power of around 1mW to avoid sample heating. Additional details on the experimental configuration are available in Ref. [44]. The Raman bands were fitted with the ~~Labspec~~ Originpro 8.0 software using pseudo-Voigt functions after careful background subtraction.

4. Results

4.1. TiC

Figure 1 presents Raman spectra recorded on TiC single and polycrystals. We have fitted the spectra with Originpro 8.0 and we put the results in green and red on the figure. TiC single crystals (Fig. 1a) exhibit two well-separated acoustic bands located at 288 cm^{-1} (TA-~~A_{1g}~~) and 386 cm^{-1} (LA-~~A_{1g}~~) and two well-separated optical bands located at 580 cm^{-1} (TO-~~T_{2g}~~) and 670 cm^{-1} (LO-~~E_g~~) [14]. Table 2 summarizes the four main Raman bands on TiC and ZrC single- and polycrystals samples.

The separation region between the highest frequency of the acoustic bands and the lowest frequency of the optical bands is about 100 cm^{-1}. The shoulder visible around 550 cm^{-1} for TiC on the virgin single crystal (see the arrow in Fig. 1a) disappears with irradiation. This band likely corresponds to a pure phonon mode of TiC which is a zone-center not found for ZrC [45]. The four main peaks increase and broaden continuously with increasing Au ion fluence, due to the damage accumulated during irradiation. Moreover, at the smallest fluence

used (2.4×10^{14} cm^{-2}), the four peaks shift towards lower frequencies. This shift is more pronounced for the ~~longitudinal~~ LA phonons (see Fig. 2). The LA/TO ratio, which is representative of the number of vacancies created by irradiation [10], increases with increasing ion fluence (see Fig. 3).

Figure 4 shows Raman spectra at high wave numbers ~~exhibiting the C-C bands~~: the disorder one (D band) at 1300-1400 cm^{-1} and the graphite one (G band) at 1550-1600 cm^{-1}. Upon irradiation, ~~free carbons are released so that~~ D and G ~~peaks~~ bands broaden, the D band becomes less intense while the G band increases gradually [47, 48]. G refers to sp2 aromatic carbons and D to defects at the edges of aromatic sheets. At the highest fluence used ($3\text{x}10^{16}$ cm^{-2}), the two peaks are not well separated. ~~After the fits and from the ratio I_D/I_G, we deduce the average in-plane size of graphitic cluster L_a determined by X-ray diffraction line widths which varies according to the empirical relation: L_a (nm) = $4.4(I_D/I_G)^{-1}$ [52]. We found around 2 nm for TiC single crystal. The graphitic cluster size is quite similar for all fluences.~~

Raman spectra on TiC polycrystals (Fig. 1b) exhibit four main ~~peaks~~ bands at values close to those obtained for single crystals: 280 cm^{-1} for TA, 398 cm^{-1} for LA, 610 cm^{-1} for TO and 700 cm^{-1} for LO. It is worth mentioning that the peak intensity increases with increasing fluence up to 9×10^{14} cm^{-2} and then decreases at 4×10^{15} cm^{-2}. The shape of the spectra is almost unchanged at all fluences but the interval between the two (TO-LO) optical bands reduces as compared to the virgin spectrum with a broadening of the peaks for both single (see fig. 6) and polycrystals. We can note that the displacements towards lower frequencies are negligible as compared to those observed for single crystals (Fig. 1a).

4.2. ZrC

Figure 6 presents Raman spectra recorded on ZrC single (a) and polycrystals (b). We have fitted the spectra with Originpro 8.0 the results are in red and green on the figure. ZrC single

crystals (Fig. 7a) exhibit two well-separated acoustic bands located at 204 cm^{-1} (TA) and 275 cm^{-1} (LA) and two well-separated optical bands located at 515 cm^{-1} (TO) and 600 cm^{-1} (LO) [14]. A comparison of the spectra of Figure 6a with those shown by Wipf and coworkers [13] indicates that the stoichiometry of virgin crystals is close to $ZrC_{0.9}$. A difference of 200 cm^{-1} is found between the region of the highest frequency of the acoustic band and that of the lowest frequency of the optical one. A shoulder appears near 325 cm^{-1} (arrow in figure 6a). Two Raman anomalies occur at ~720 cm^{-1} (additive TO+TA) and at ~820 cm^{-1} (additive TA+LO). The four main peaks increase in intensity and broaden with increasing ion fluence due to the damage accumulation. A shift towards low frequencies is observed for the four peaks (Fig. 7) similarly to TiC but for a higher fluence (2.6×10^{15} cm^{-2}). This shift is more important for longitudinal optical mode. The broadening of the peaks induces a reduction of the frequency interval for each doublet (especially for optical modes), as compared to the virgin spectra. The ratio LA/TO representative of the number of vacancies created by irradiation [10] increases with fluence (Fig. 3).

Figure 9 shows the ~~C-C bands Disorder~~ D band ~~(D)~~ at 1300-1400 cm^{-1} and the ~~Graphitic~~ band ~~(G)~~ at 1550-1600 cm^{-1}. For the first fluence of 2.4×10^{14} cm^{-2}, D and G peaks are separated and then broaden with increasing fluence. At the highest fluence used ($3x10^{16}$ cm^{-2}), D and G bands are convoluted and form one totally amorphous peak with a third contribution [47, 48]. ~~On figure 5, we found that the graphitic cluster size is around 3.5 nm. The graphitic cluster size decreases with fluence.~~

Raman spectra on ZrC polycrystals (Fig. 6b) exhibit four main peaks at values close to those obtained for single crystals: 210 cm^{-1} for TA, 280 cm^{-1} for LA, 520 cm^{-1} for TO and 615 cm^{-1} for LO. The peak intensity increases with increasing ion fluence. A comparison of the spectrum recorded on the virgin sample with those obtained by Wipf [13] indicates that the stoichiometry of ZrC polycrystals corresponds to $ZrC_{0.96}$. The prominent TO peak at 540 cm^{-1}

disappears at the first irradiation fluence and the acoustical peaks are very weak. The peak at 360 cm^{-1}, that is visible on the spectrum recorded on the virgin sample, decreases upon irradiation. The TA band which is very weak on virgin sample increases immediately with the lowest fluence of 2×10^{13} cm^{-2}. After that, the shape of the spectrum seems to be conserved for all fluences but the interval between the two optical bands (TO-LO) appears to be reduced with the broadening of the peaks. No clear frequency displacement towards lower frequencies is observed for polycrystals.

Figure 9 presents a TEM image recorded on a TiC thin sample prepared from a TiC single crystal irradiated at 1.2×10^{15} cm^2 (the beginning of the second step in damage build-up of TiC [36]) by using a Focused Ion Beam (FIB). Dislocation loops are clearly created upon irradiation, with an average loop size of < 4 nm. ~~The graphitic cluster size of 3.5 nm is in good agreement with the TEM observation (Fig. 10).~~

5. Discussion

Raman spectra of such disordered and non-stoichiometric materials reflect the VDOS including acoustic and optical branches. A direct relationship exists between the VDOS ~~phonon density of state diagrams~~ of TiC_{1-x} and ZrC_{1-x} and the Raman spectrum as discussed by Jockym [4] and Schwarz [38]. ~~Neckel [4], Dridi [5], Zhukov [9] and Schwarz [43].~~

~~In $TiC_{(1-x)}$, the active Raman bands are respectively identified as A_{1g}, E_g and T_{2g}. In this pioneering work, Klein [44] specifies that the acoustical phonons (A_{1g}) located in the Raman shift region 200–450 cm^{-1} are related to the motion of Ti atoms, while the optical phonons (T_{2g} and E_g) located between 500 and 800 cm^{-1} correspond to the motion of C atoms. The relative intensity varies in the following order: $E_g > A_{1g} > T_{2g}$.~~ The intensity of both types of bands (acoustic~~al~~ and optical) increases with the increase of the stoichiometric deviation (x). This tendency was also observed by Lohse for TiC synthesized by ball milling [40, 41]. ~~Peak~~

~~shoulders may appear in the vicinity of A_{1g} and T_{2g} bands when *x* tends to zero (stoichiometric); this occurrence is called two-phonon Raman anomaly [17].~~

The general features discussed above for TiC_{1-x} Raman spectra also apply to ZrC_{1-x} as stated by Wipf [13]. Two well-separated acoustic bands are located at 200-210 cm^{-1} (A1) and at 270–280 cm^{-1} (A2) and two well-separated optical bands are located at 530–540 cm^{-1} (O1) and at 600 cm^{-1} (O2) for ZrC [18]. Nevertheless, a specific feature is worth mentioning: the ~~separation region~~ gap between the highest frequency of the acoustical band located near 300 cm^{-1} and the lowest frequency of the optical one appearing close to 500 cm^{-1} is wider than ~~that existing~~ for TiC. This property is due to the higher mass difference between metal and non-metal atoms in ZrC as compared to TiC [13].

The similarities and differences observed in the Raman spectra obtained for TiC and ZrC virgin samples derive from both the shape of their VDOS ~~density of states and the band structure diagrams~~. The separation between the highest frequency of the acoustic band and the lowest frequency of the optical one is larger for ZrC than for TiC, due to the higher mass difference between metal and non-metal atoms in ZrC as compared to TiC. ~~This result is in agreement with the width difference measured between the two DOS blocks of peaks located on both sides of their respective Fermi level [9,18,53].~~

Whatever the Au ion fluence used, the four main peaks due to acoustic and optical phonons are conserved. This means that the amorphization is not reached for both carbides. This observation is in fairly good agreement with the results obtained by RBS-C ~~Rutherford backscattering spectrometry~~ experiments conducted in channeling mode [19] where the aligned spectra never reach the random level, meaning that a total disorder is never attained in the irradiated thickness. The LA/TO ratios increase with increasing fluence for both TiC and ZrC, namely with the increasing number of vacancies created by irradiation, as shown by Chen [10]. The shape of the Raman spectra recorded on TiC and ZrC single crystals at 3×10^{16}

cm^{-2} is similar to that obtained at 4×10^{15} cm^{-2} for polycrystals. This result shows that polycrystals samples are more radiation tolerant than single crystals probably due to the role of defect annihilation sinks played by grain boundaries.

The displacement towards lower frequencies observed on Raman spectra when the Au ion fluence increases, which may reveal the occurrence of an internal stress induced by irradiation, is more pronounced for single crystals than for polycrystals. Such a result may be due to the relaxation of the internal stress by the presence of grain boundaries in polycrystals. Another explanation for this shift would be due to a decrease of the stoichiometry similar to that already observed by Wipf [13]. In single crystals this shift starts at higher fluence for ZrC than for TiC. Actually, for TiC this shift is visible at the weakest fluence of 2.4×10^{14} cm^{-2}, whereas it occurs above 1.4×10^{15} cm^{-2} for ZrC. This result indicates that ZrC is more stress resistant than TiC upon irradiation. Such a conclusion may also be derived from XRD experiments [19] where TiC exhibits an elastic strain higher (0.44 %) than that of ZrC (0.38 %).

The gap between the two optical bands for each carbide increases gradually with increasing ion fluence. This phenomenon underlines the fact that peaks broaden upon irradiation. It confirms that the disorder increases due to the increasing number of carbon vacancies ~~(optical lines correspond to the C element), while C-C band intensity increasing more and more intense with increasing fluence.~~ The two broad bands located at 1400 and 1600 cm^{-1} (Figures 4 and 8), which are not found for virgin samples (no free carbon) and appear only after irradiation, reveal the formation of carbon aggregates ~~clusters~~ clearly increasing for the highest fluence~~. As a matter of fact, the decrease in intensity of the D band and the increase of the G band mean that the disordered carbon created by irradiation becomes graphitic upon irradiation (ordered carbon). The size of such graphitic carbon clusters, deduced from the ratio of D and G band intensities, is seen to decrease with fluence, at least for ZrC from 4 nm to 1.5~~

~~nm (Figure 5). This size is consistent with the size of dislocation loops (< 4 nm) found by TEM at a fluence of 1.2×10^{15} cm^{-2} in TiC (Fig. 10).~~ For different orientations, the lattice parameter and structure have been checked by electron diffraction. The crystalline structure Fm3m still unchanged after irradiation for both carbides. Further High Resolution TEM studies are definitely needed to confirm that these loops are interstitial carbon loops.

As of the four main peaks remain present, we can deduce that TiC and ZrC single or polycrystals are not amorphized even at the highest fluence used. In both carbides, the nature of defects created upon irradiation corresponds to the first two steps of the damage build-up as observed by Motta and coworkers [31], Gosset [23, 24] and Pellegrino and coworkers [36]: (i) the creation of point defects (Frenkel pairs) at low fluences (below ~10^{15} cm^{-2}), and (ii) the formation of extended defects (interstitial and/or vacancy clusters and dislocation loops) when the fluence is increased above 10^{15} cm^{-2} (see Figure 9).

6- Conclusion

For ~~all samples and all structures~~ single crystals and polycrystalline samples of TiC_{1-x} and ZrC_{1-x}, 1.2 MeV Au ion irradiation induces point defects like Frenkel pairs at lowest fluence and ~~more~~ extended defects at the highest fluence, like ~~dislocations and~~ dislocation loops showed by TEM observations. ~~But~~ Yet no amorphization is observed in any case. The ~~variation~~ increase of LA/TO band ratio in Raman spectra with fluence for all samples indicates that the number of carbon vacancies increases. ~~and may modify the local stoichiometry~~. At the same time, widths of the ~~peaks~~ Raman bands increase and ~~the C-C~~ carbon related bands appear ~~too (free carbon) and become graphitic~~ with increasing fluence. ~~A local order takes place with carbon interstitial defects and form clusters. The size of the graphitic clusters does not exceed 4 nm. Cluster size decreases with fluence for ZrC from 4 nm to 1.5 nm but there is no change for TiC (around 2 nm). This phenomenon is also put in~~

~~evidence with TEM observation. But High Resolution TEM is needed to learn more about the nature of the loops at higher fluence.~~

Acknowledgements

I would like to thank Marion Le Flem for supplying us with polycrystals (TiC and ZrC), Daniel Brimbal and Marie Loyer-Prost for the FIB preparation and TEM observations. The authors are gratefull to both JANNUS teams at Saclay and Orsay for their cooperation during all the irradiations.

References

[1] High temperature gas cooled reactor fuels and material&ls, Report IAEA-TECDOC-1645, International Atomic Energy Agency, Vienne, 2010.

[2] B.D. Wirth, K. Nordlund, D.G. Whyte, D. Xu, MRS Bull. 36 (2011) 216–222.

[3] T.R. Allen, K. Sridharan, L. Tan, W.E. Windes, J.I. Cole, D.C. Crawford, G.S. Was, Nucl. Technol. 162 (2008) 342–357.

~~[4] A Neckel, P Rastl, R Eibler, P Weinberger, K Schwarz, J. Phys. C: Solid State Phys. 9 (1976) 579-592.~~

~~[5] Z. Dridi, B. Bouhafs, P. Ruterana, H. Aourag, J. Phys. Condens. Matter 14 (2002) 10237–10249~~.

[4] P.T. Jochym, K. Parlinski, Europ. Phys. J. B 15 (2000) 265-268.

~~[7] Zengtao Lv, Haiquan Hu, Cheng Wu, Shouxin Cui, Guiqing Zhang, Wenxia Feng, Physica B 406 (2011) 2750–2754.~~

~~[8] V.A. Gurbanov, A.L. Ivanovsky, V.P. Zhukov, "Electronic Structure of Refractory Carbides and Nitrides", Cambridge University Press, Cambridge, 1994.~~

~~[9] V.P. Zhukov, V.A. Gubanov, O. Jepsen, N.E. Christensen, O.K. Andersen, J. Phys. Chem. Sol. 49 (1988) 841-849.~~

[5] Nguyen Xuan Xinh, A.A. Maradudin, R.A. Coldwell-Horsfall, J. Phys. France 26 (1965) 717-735.

[6] W. Spengler, R. Kaiser, H. Bilz, Solid State Communications 17 (1975) 19-22.

[7] W. Spengler, R. Kaiser, Solid State Communications 18 (1976) 881-884.

[8] W. Spengler, R. Kaiser, A.N. Christensen, G. Müller-Vogt, Phys. Rev. B, 17 (1978) 1095-1101.

[9] W. Kress, P. Roedhammer, H. Bilz, W.D. Teuchert, A.N. Christensen, Phys. Rev. B 17 (1978) 111-113.

[10] C.C. Chen, N.T. Liang, W.S. Tse, I.Y. Chen, J.G. Duh, Chinese J. Phys. 32 (1994) 205-210.

[11] M. Stoehr, H. S. Seo, I. Petrov, J.E. Greene, J. Appl. Phys. 99 (2006) 043507.

[12] M.V. Klein, J.A. Holy, W.S. Williams, Phys. Rev. B 17 (1978) 1546-1556.

[13] H. Wipf, M.V. Klein, W.S. Williams, Physica Status Solidi b 108 (1981) 489-499.

[14] S. Pellegrino, L. Thomé, A. Debelle, S. Miro, P. Trocellier, Nucl. Instrum. Meth. Phys. Res. B 327 (2014) 103–107.

[15] S. Agarwal, P. Trocellier, S. Vaubaillon, S. Miro, J. Nucl. Mater. 448 (2014) 144–152.

[16] G. Das, D.K. Chatterjee, H.A. Lipsitt, J. Mater. Sci. 16 (1981) 3283-3291.

[17] K. Hojou, H. Otsu, S. Furuno, N. Sasajima, K. Izui, J. Nucl. Mater. 239 (1996) 279-283.

[18] K. Hojou, H. Otsu, S. Furuno, N. Sasajima, K. Izui, Nucl. Instrum. Meth. Phys. Res. B 127/128 (1997) 203-207.

[19] K. Hojou, H. Otsu, S. Furuno, N. Kushita, N. Sasajima, K. Izui, Nucl. Instrum. Meth. Phys. Res. B 148 (1999) 720-725.

[20] C.A. Dickerson, Yong Yang, T.R. Allen, J. Nucl. Mater. 424 (2012) 62-68.

[21] M.L. Taubin, Translated from Atomnaya Energiya, 69 (1990) 176-177.

[22] M.L. Taubin, Translated from Atomnaya Energiya, 70 (1991) 55-56.

[23] D. Gosset, M. Dollé, D. Simeone, G. Baldinozzi, L. Thomé, J. Nucl. Mater. 373 (2008) 123-129.

[24] D. Gosset, M. Dollé, D. Simeone, G. Baldinozzi, L. Thomé, Nucl. Instrum. Meth. Phys. Res. B 266 (2008) 2801-2805.

[25] Jian Gan, M.K. Meyer, R.C. Birtcher, T.R. Allen, J. ASTM International 3 (2006)12376

[26] Jian Gan, Yong Yang, C.A. Dickerson, T.R. Allen, J. Nucl. Mater. 389 (2009) 317-325.

[27] L.L. Snead, Y. Katoh, Sosuke Kondo, J. Nucl. Mater. 399 (2010) 200-207.

[28] G. H. Reynolds, J. C. Janvier, J. L. Kaae, J. P. Morlevat, J. Nucl. Mater. 62 (1976) 9-16.

[29] Sungtae Kim, I. Szlufarska, D. Morgan, J. Appl. Phys. 107 (2010) 053521.

[30] H.F. Jackson, W.E. Lee, in Comprehensive Nucl. Mater. , Chapter 2-13, pp. 339-372, Elsevier, Amsterdam, 2012.

[31] A. Motta, DOE-NEUP 10-679, Final Report, 2013.

[32] Y. Katoh, G. Vasudevamurthy, T. Nozawa, L.L. Snead, J. Nucl. Mater. 441 (2013) 718-742.

[33] C. Jensen, M. Chirtoc, J. S. Antoniow, H. Ban, Int. J. Thermophys. 34 (2013) 597-608.

[34] Y. Huang, B.R. Maier, T.R. Allen, Nucl. Engin. Design 277 (2014) 55–63.

[35] S. Pellegrino, L. Thomé, A. Debelle, S. Miro, P. Trocellier, Nucl. Instrum. Meth. Phys. Res. B 307 (2013) 294–298.

[36] S. Pellegrino, L. Thomé, A. Debelle, S. Miro, P. Trocellier, Nucl. Instrum. Meth. Phys. Res. B 327 (2014) 103–107.

[37] L. W. Hobbs, Nucl. Instrum. Meth. Phys. Res. B 91 (1994) 30-42.

[38] K. Schwarz, H. Ripplinger, A. Neckel, Z Phys. B Condensed Matter 48 (1982) 79-87.

[39] M.V. Klein, Phys. Rev. B 24 (1981) 4208-4223.

[40] B.H. Lohse, A. Calka, D. Wexler, J. Appl. Phys. 97 (2005) 114912.

[41] B.H. Lohse, A. Calka, D. Wexler, J. Alloys Comp. 434-435 (2007) 405-409.

[42] P. Trocellier, S. Miro, Y. Serruys, S. Vaubaillon, S. Pellegrino, S. Agarwal, S. Moll, L. Beck, Nucl. Instrum. Meth. Phys. Res. B 331 (2014) 55–64.

[43] J.F. Ziegler, SRIM (2013), <http://www.srim.org>.

[44] S. Miro, G. Velisa, L. Thomé, P. Trocellier, Y. Serruys, A. Debelle, F. Garrido, J. Raman Spectrosc. 45 (2014) 481–486.

[45] W. Weber, Phys. Rev. B 8, (1973), 5082, 455.

[46] Tuinstra and Koenig, 1970

[47] S. Urbonaite, L. Hälldahl, G. Svenson, Carbon 46 (2008) 1942-1947.

[48] L. Zhang, R. V. Koka, Mater. Chem. Phys. 57 (1998) 23-32.

~~[52] J. M. Costantini, F. Couvreur, J. P. Salvetat, S. Bouffard, Nucl. Instrum. Meth. Phys. Res. B 194 (2002) 132-140.~~

Figure Captions

Figure 1: Raman spectra on TiC single crystals fitted curves in green and red (a) and TiC polycrystals (b) irradiated with Au ions at the indicated fluences (cm^{-2}).

Figure 2: Shift of the four main Raman peaks ($\Delta\nu/\nu$) in TiC as a function of the Au fluence (in logarithmic scale).

Figure 3: Ratio LA/TO as a function of the Au fluence for TiC and ZrC single and polycrystals. The red curve represents the 2^{nd} degree polynomial fit with all experimental data.

Figure 4: Raman spectra at high wave numbers representing the C-C bands for TiC single crystals irradiated with 1.2 MeV Au ions at the indicated fluences. Red and green curves are Gaussian fits of the experimental peaks.

Figure 5: Gap between TO and LO bands for TiC and ZrC single and polycrystals.

Figure 6: Raman spectra on ZrC single crystals, fitted curves in green and red (a) and ZrC polycrystals (b) irradiated with Au ions at the indicated fluences (cm^{-2}).

Figure 7: Shift of the four main Raman peaks ($\Delta\nu/\nu$) in ZrC as a function of the Au fluence (in logarithmic scale).

Figure 8: Raman spectra at high wave numbers representing the C-C bands for ZrC single crystals irradiated with 1.2 MeV Au ions at the indicated fluences. Red and green curves are Gaussian fits of the experimental peaks.

Figure 9: TEM image of a TiC thin film prepared by FIB irradiated at 1.2×10^{15} cm^{-2} (~7 dpa) with 1.2 MeV Au ions. White arrows indicate the presence of dislocation loops.

Figure 1a

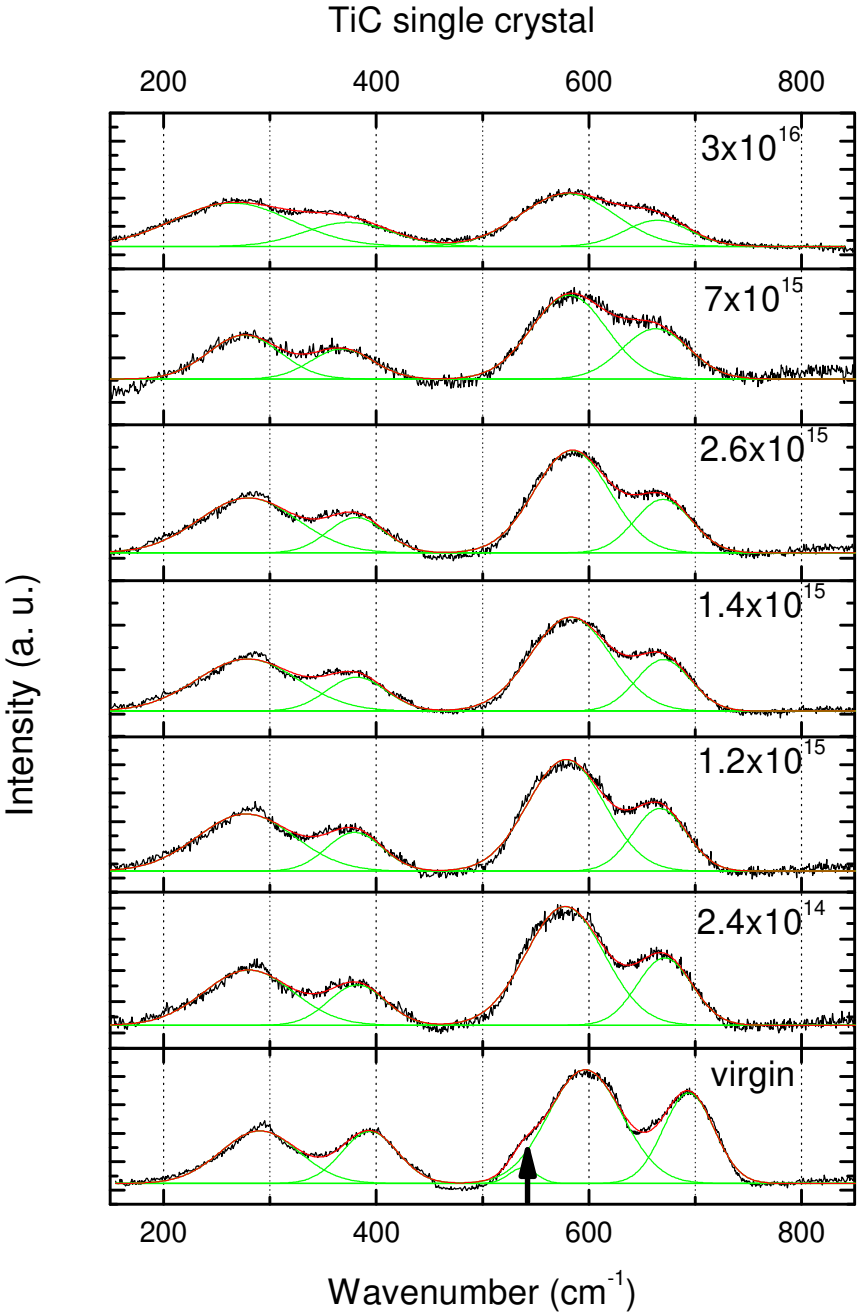
TiC single crystal
200
400
600
800
3x10^16
7x10^15
2.6x10^15
1.4x10^15
1.2x10^15
2.4x10^14
virgin
Intensity (a. u.)
Wavenumber (cm^-1)

Figure 1b

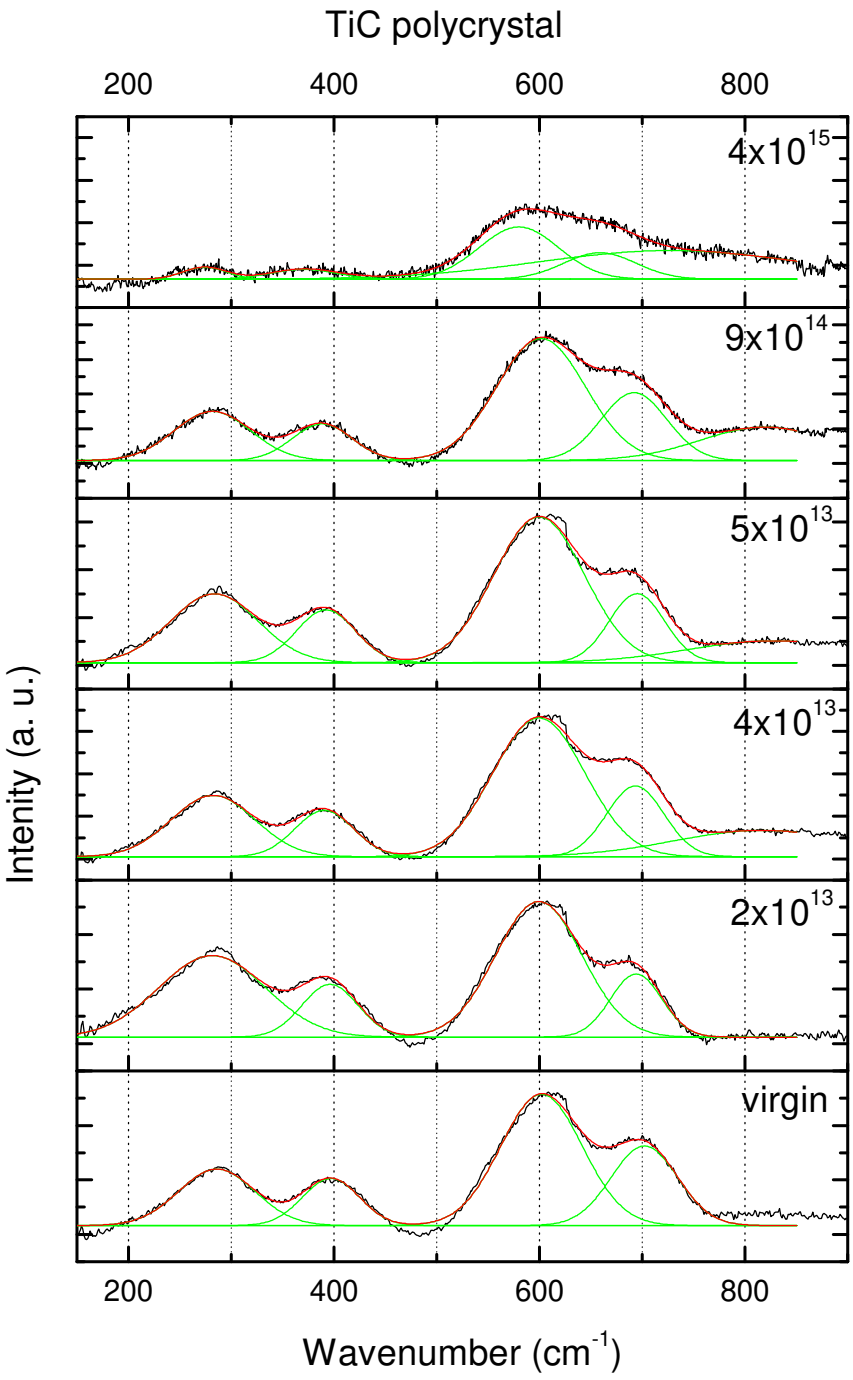
TiC polycrystal
200
400
600
800
4x10^15
9x10^14
5x10^13
4x10^13
2x10^13
virgin
Intenity (a. u.)
Wavenumber (cm^-1)

Figure 2

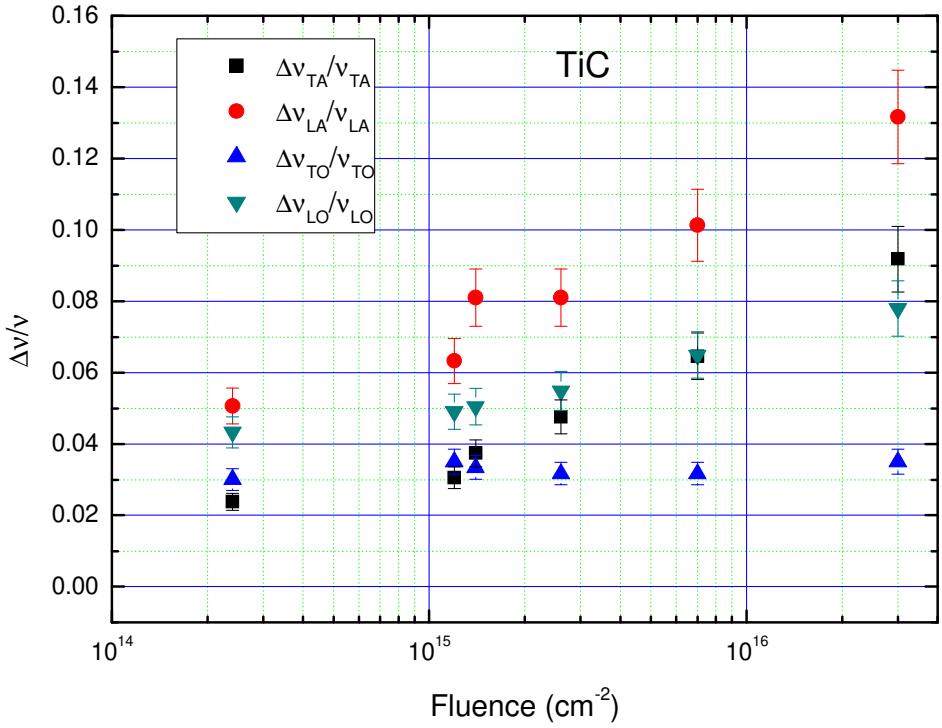
TiC
$\Delta\nu_{TA}/\nu_{TA}$
$\Delta\nu_{LA}/\nu_{LA}$
$\Delta\nu_{TO}/\nu_{TO}$
$\Delta\nu_{LO}/\nu_{LO}$
$\Delta\nu/\nu$
0.16
0.14
0.12
0.10
0.08
0.06
0.04
0.02
0.00
10^{14}
10^{15}
10^{16}
Fluence (cm^{-2})

Figure 3

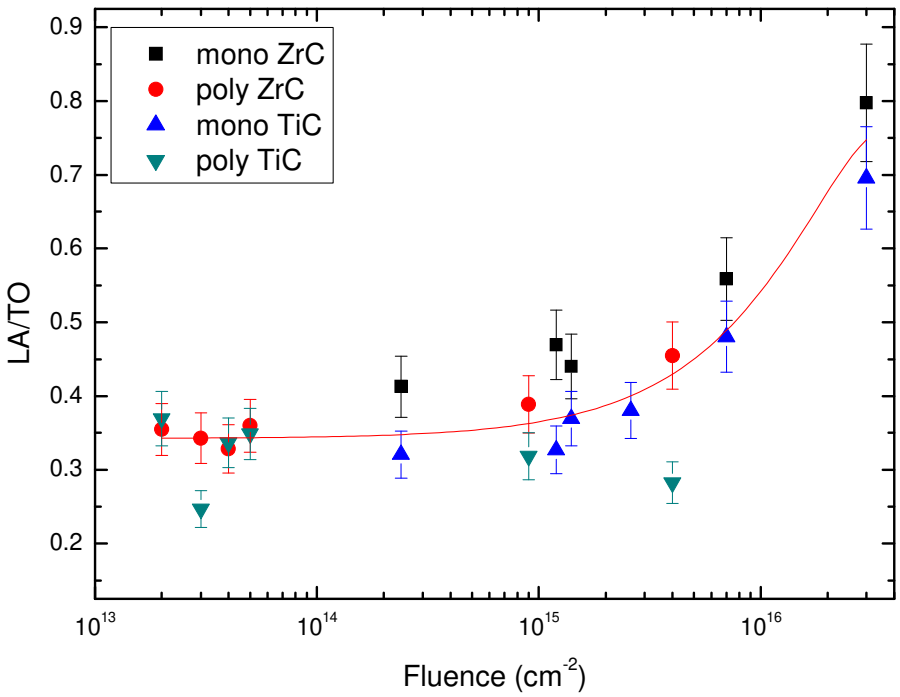
mono ZrC
poly ZrC
mono TiC
poly TiC
LA/TO
0.9
0.8
0.7
0.6
0.5
0.4
0.3
0.2
10^{13}
10^{14}
10^{15}
10^{16}
Fluence (cm^{-2})

Figure 4

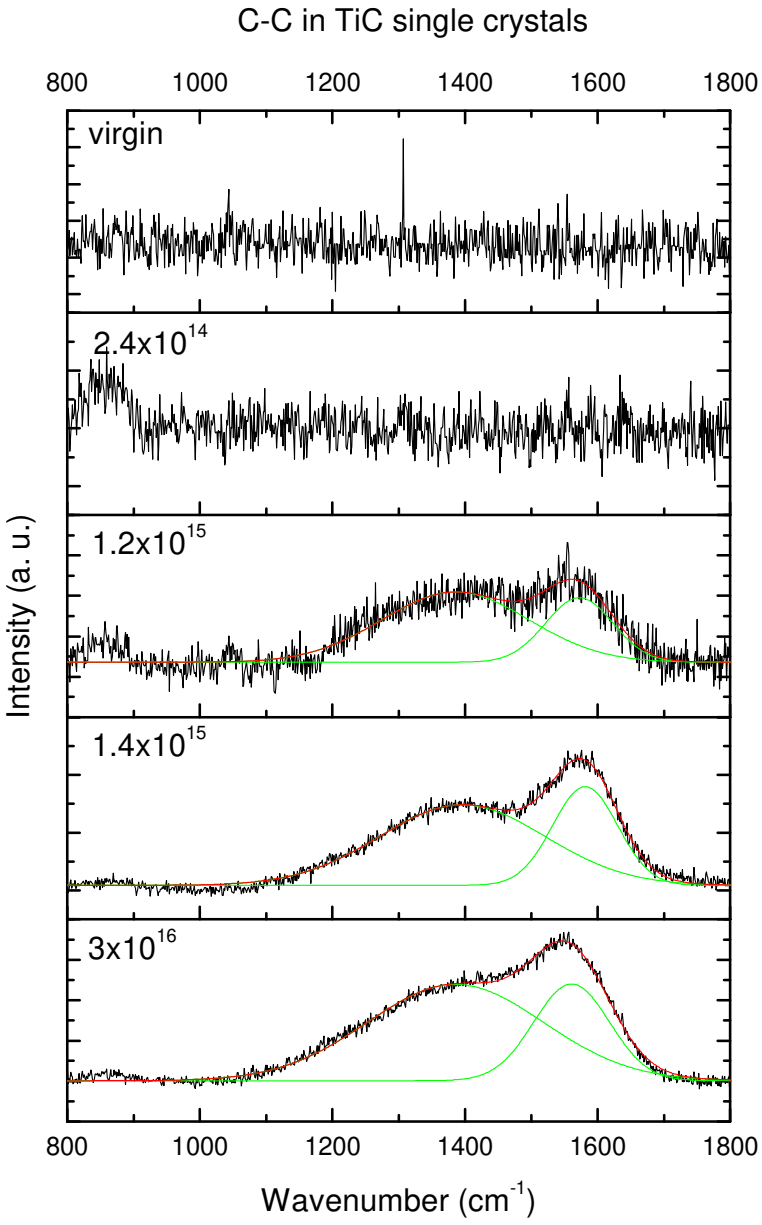
C-C in TiC single crystals
800
1000
1200
1400
1600
1800
virgin
2.4x10^14
1.2x10^15
1.4x10^15
3x10^16
Intensity (a. u.)
Wavenumber (cm^-1)

Figure 5

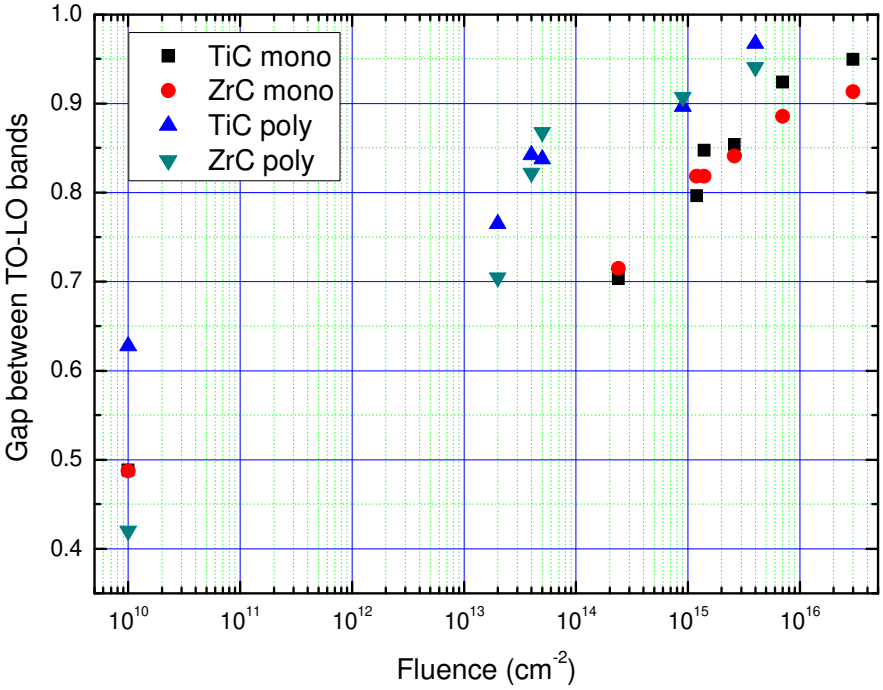
TiC mono
ZrC mono
TiC poly
ZrC poly
Gap between TO-LO bands
Fluence (cm-2)
1.0
0.9
0.8
0.7
0.6
0.5
0.4
10^10
10^11
10^12
10^13
10^14
10^15
10^16

Figure 6a

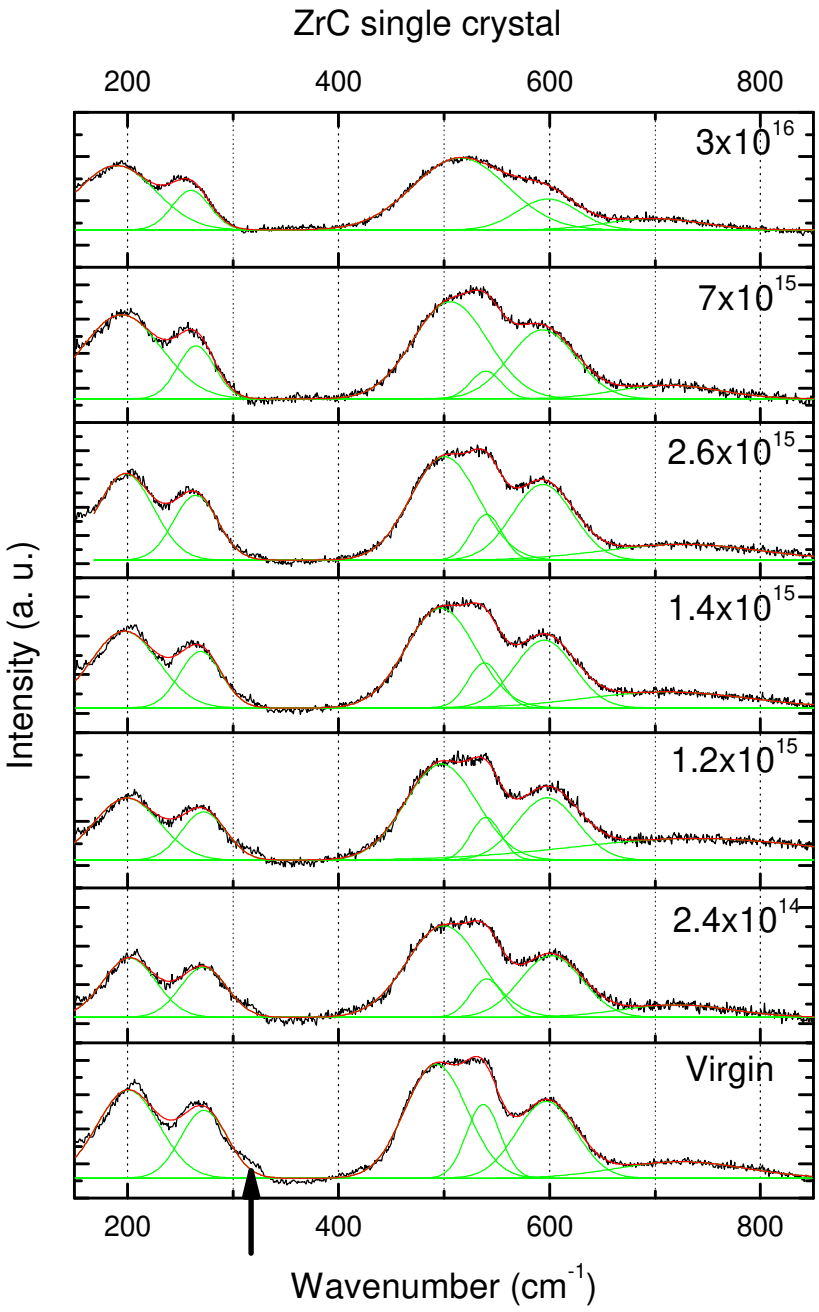
ZrC single crystal
200
400
600
800
3x10^16
7x10^15
2.6x10^15
1.4x10^15
1.2x10^15
2.4x10^14
Virgin
Intensity (a. u.)
Wavenumber (cm^-1)

Figure 6b

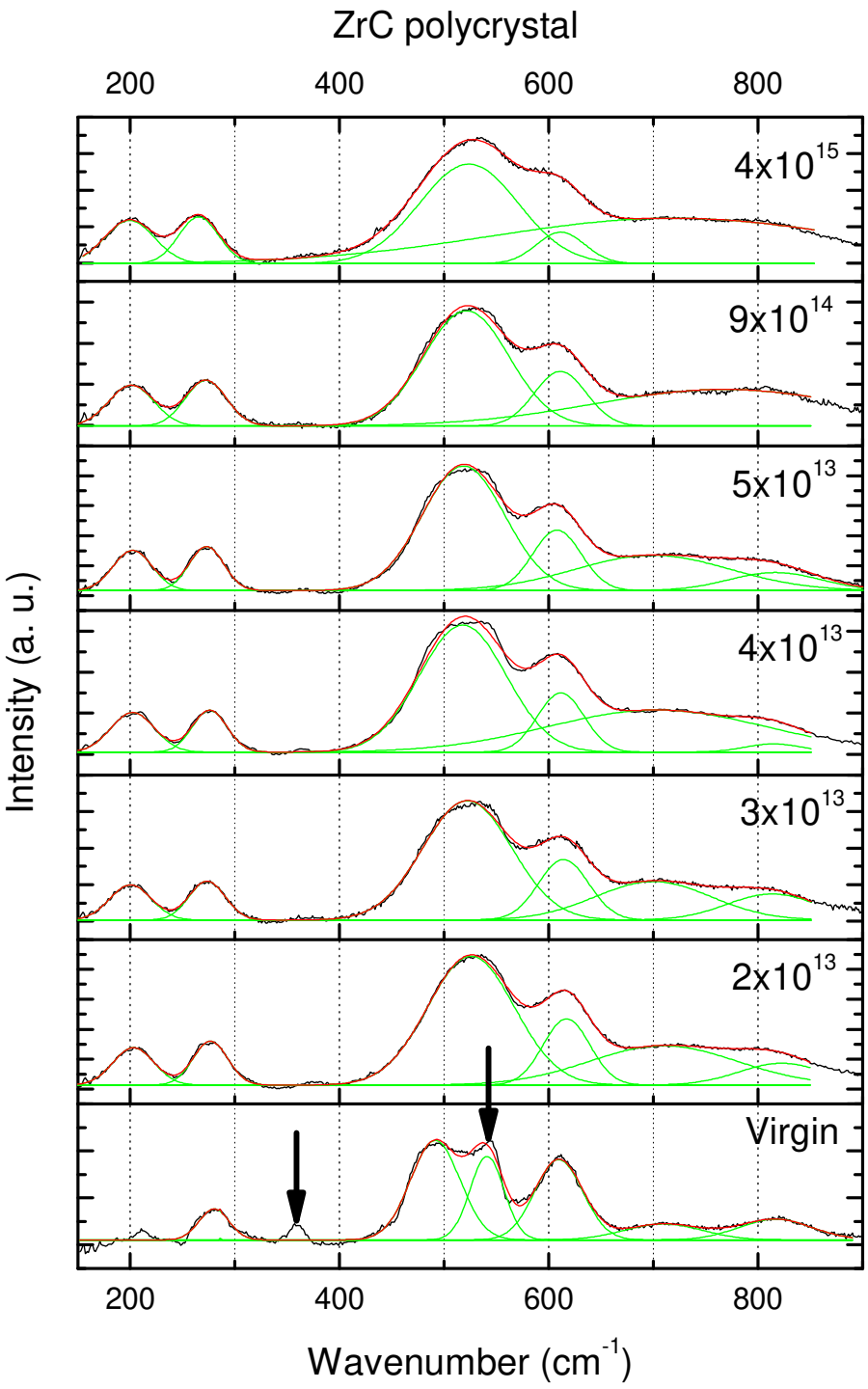
ZrC polycrystal
200
400
600
800
4x10^15
9x10^14
5x10^13
4x10^13
3x10^13
2x10^13
Virgin
Intensity (a. u.)
Wavenumber (cm^-1)

Figure 7

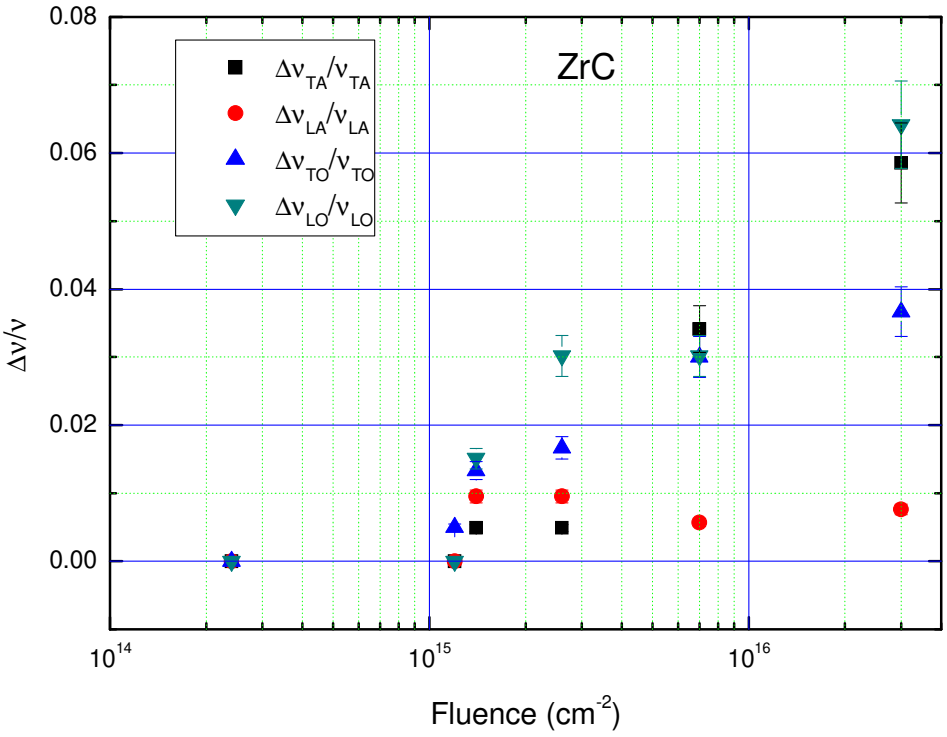
ZrC
$\Delta\nu_{TA}/\nu_{TA}$
$\Delta\nu_{LA}/\nu_{LA}$
$\Delta\nu_{TO}/\nu_{TO}$
$\Delta\nu_{LO}/\nu_{LO}$
0.08
0.06
0.04
0.02
0.00
$\Delta\nu/\nu$
10^{14}
10^{15}
10^{16}
Fluence (cm^{-2})

Figure 8

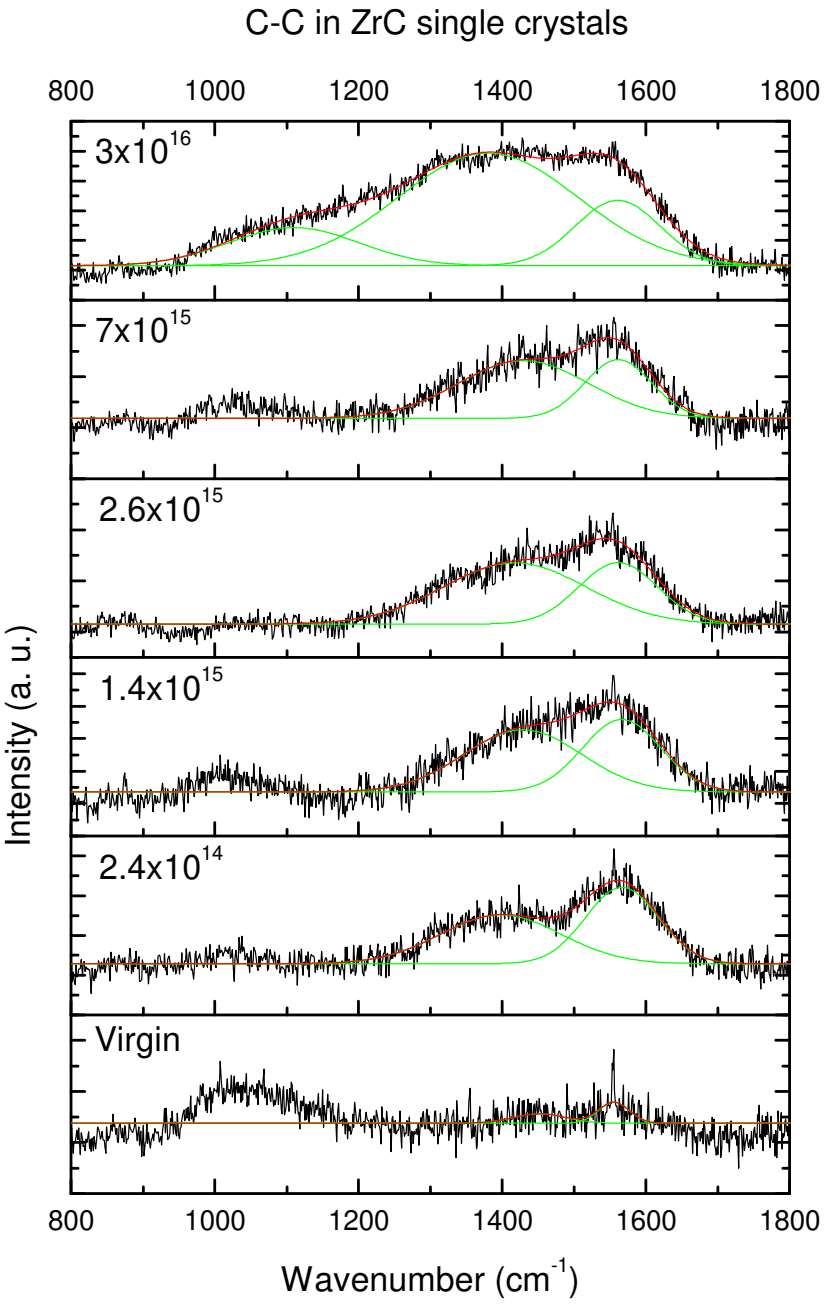
C-C in ZrC single crystals
800
1000
1200
1400
1600
1800
3x10^16
7x10^15
2.6x10^15
1.4x10^15
2.4x10^14
Virgin
Intensity (a. u.)
Wavenumber (cm^-1)

Figure 9

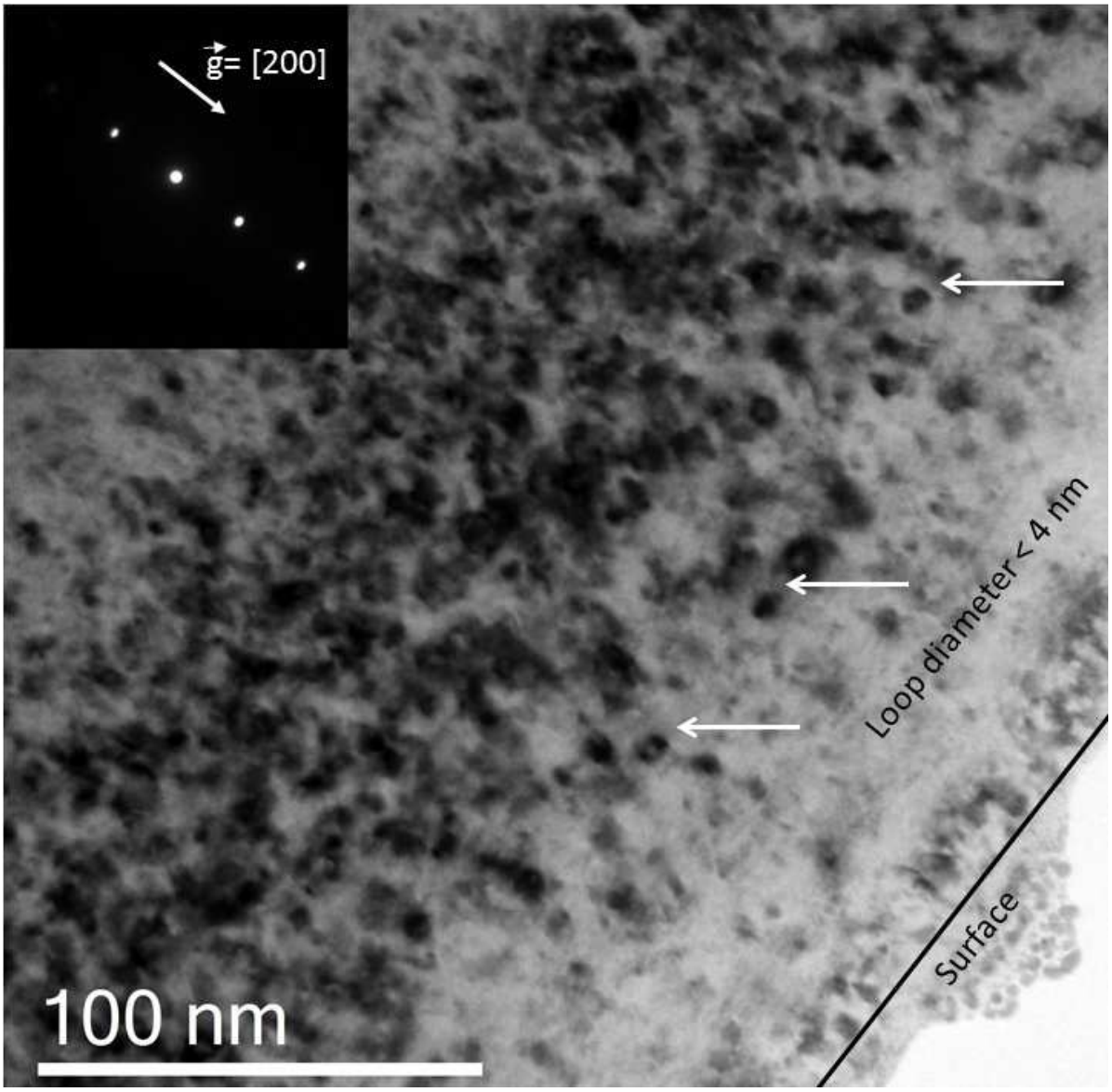

Table caption

Table 1: Parameters for 1.2 MeV Au ion irradiation of TiC and ZrC (obtained from SRIM simulations [48].

Table 2: Wavenumbers of the main Raman bands for TiC and ZrC single and polycrystals.

Table 1

Sample	TiC	ZrC
Projected Range R_p (nm)	151	141
Range straggling ΔR_p (nm)	35	44
Fluence (cm^{-2})	2×10^{13}-2×10^{14} 4×10^{15}-3×10^{16}	2×10^{13}-2×10^{14} 4×10^{15}-3×10^{16}
dpa*	0.08-0.83 16.5-124	0.12-1.22 24-182
$(dE/dx)_{nuclear}$ (keV/μm)	5300	5900
$(dE/dx)_{electronic}$(keV/μm)	3130	2670

*to calculate the number of dpa, we have used SRIM in Full damage cascades mode. For displacement energies we have used E_d =50 eV for Zr and 30 eV for C; and $E_{d=}$ 40 eV for Ti and 30 eV for C. For densities number of atoms per cm^3, we have used 4.93 g/cm^3 for TiC and 6.9 g/cm^3 for ZrC.

Table 2

sample	type	Acoustic (cm^{-1})		Optical (cm^{-1})	
TiC	Single	288	386	580	670
	Poly	280	398	610	700
ZrC	Single	204	275	515	600
	Poly	210	280	520	615